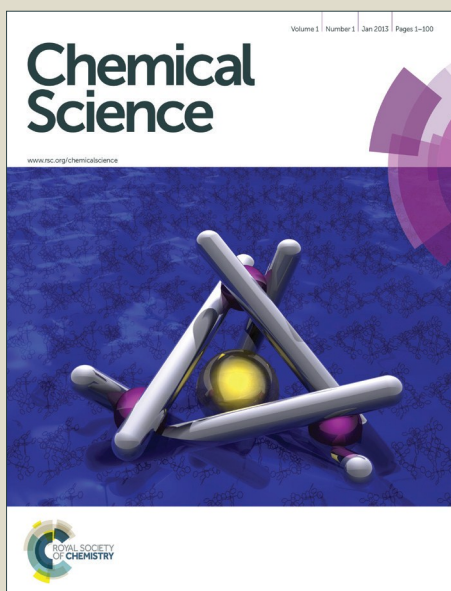


Chemical Science

Accepted Manuscript



This is an *Accepted Manuscript*, which has been through the Royal Society of Chemistry peer review process and has been accepted for publication.

Accepted Manuscripts are published online shortly after acceptance, before technical editing, formatting and proof reading. Using this free service, authors can make their results available to the community, in citable form, before we publish the edited article. We will replace this *Accepted Manuscript* with the edited and formatted *Advance Article* as soon as it is available.

You can find more information about *Accepted Manuscripts* in the [Information for Authors](#).

Please note that technical editing may introduce minor changes to the text and/or graphics, which may alter content. The journal's standard [Terms & Conditions](#) and the [Ethical guidelines](#) still apply. In no event shall the Royal Society of Chemistry be held responsible for any errors or omissions in this *Accepted Manuscript* or any consequences arising from the use of any information it contains.



Self-Assembly of 2D MnO₂ Nanosheets into High-Purity Aerogels with Ultralow Density†

Zhenning Liu,^a Kongliang Xu,^a Ping She,^a Shengyan Yin,^b Xuedong Zhu^a and Hang Sun^{*a}

Received 00th January 20xx,
Accepted 00th January 20xx

DOI: 10.1039/x0xx00000x

www.rsc.org/

Self-assembling inorganic nanoparticles (NPs) into macroscopic three dimensional (3D) architectures often requires the assistance of organic components, leaving residual organics in the resultant. In this work, organic-free MnO₂ aerogels with ultralow density have been achieved by self-assembly of two dimensional (2D) MnO₂ nanosheets via an ice-templating approach. To the authors' best knowledge, it is the first reported case of constructing high-purity inorganic aerogel from preformed NPs without using any functionalization or stabilization agents. Moreover, it has been demonstrated that ultralight MnO₂ aerogel with a density as low as ~0.53 mg cm⁻³ can be well obtained by such an approach, which is the lightest metal oxide aerogel to date. The successful formation of the aerogel can be attributed to the enhanced van der Waals force between the 2D building blocks that have been more closely and more orderly arranged by squeezing ice crystals during freezing process. Hence, this work shows a pioneering example of assembling inorganic NPs into aerogels only relying on the weak interaction between NPs (*e.g.* van der Waals force). It has also been demonstrated that the obtained MnO₂ aerogel can function as an effective absorbent for toxic reducing gas, owing to its strong oxidation ability and high porosity. The herein presented strategy holds good potential to be applied to the fabrication of other high-purity inorganic aerogels, especially for those with 2D building blocks readily available.

Introduction

Self-assembling inorganic nanoparticles (NPs) into macroscopic three dimensional (3D) architectures is an important bottom-up strategy in nano-research, bridging the gap between individual NPs and the structures suitable for practical applications.¹⁻³ Aerogels are a class of 3D porous architectures with low density, large open pores and high surface area,⁴⁻⁷ which imparts them a broad range of applications including thermal insulation, toxicant absorption, energy conversion and storage, catalyst support, *etc.*⁸⁻¹⁶ Assembly of inorganic (*e.g.* metal, oxide, chalcogenide, pnictide) NPs into such functional aerogels has attracted broad attention in recent years.¹⁷⁻²¹ The resultant aerogels usually exhibit hierarchical structures with controlled crystallinity and composition, which can afford the chemical and physical features of NPs in addition to typical properties of macro porous materials, and often integrate various properties in one material.

A common strategy of organizing NPs into a 3D percolating

network is to install organic functionalities onto the surface of inorganic NPs to effect cross-linking. For instances, organics, such as 2-[2-(2-methoxyethoxy) ethoxy] acetic acid, polyethylenimine, sodium dodecyl benzene sulfonate (SDBS), sodium cholate (SC), *etc.* have been utilized to assist aerogel formation from preformed inorganic NPs.^{18, 22, 23} Unfortunately, since the assembling force provided by these exogenous organic components is critical to the construction of such aerogels, the obtained aerogels are indeed a hybrid of organic and inorganic materials and often incur unwanted property impairment caused by the cross-linkers. Alternatively, controlled destabilization of NPs in dispersion (*e.g.* partial removal of the surface stabilizing agent by oxidation) has also been adopted to induce self-assembly of NPs into inorganic aerogels, such as the aerogels of chalcogenide,¹⁹ pnictide,¹⁷ noble metal,^{24, 25} *etc.* Nonetheless, the aerogels formed by destabilization normally contain trace amount of impurities as a consequence of incomplete removal of surface stabilizing agents and suffer from reduced performance (*e.g.* charge transport and thermal stability) due to the residual organics.²⁴ Hence, an approach to fabricate high-purity inorganic aerogels from preformed NPs is still in great need.

Ice-templating is an inexpensive, convenient and scalable technique that exploits endogenous ice crystals as templates to shape and press building blocks to achieve a desired structure.²⁶⁻²⁸ Recently, aerogels of Ag, Cu and MnO₂ have been constructed by ice-templating from polyvinylpyrrolidone

^a Key Laboratory of Bionic Engineering (Ministry of Education), College of Biological and Agricultural Engineering, Jilin University, Changchun, Jilin 130022, P. R. China. E-mail: sunhang@jlu.edu.cn

^b State Key Laboratory on Integrated Optoelectronics, College of Electronic Science and Engineering, Jilin University, Changchun, Jilin 130012, P. R. China.

† Electronic Supplementary Information (ESI) available: See DOI: 10.1039/x0xx00000x

(PVP)-stabilized Ag/Cu nanowires and dimethylformamide (DMF)-capped MnO₂ nanoflowers, respectively.²⁹⁻³¹ Yet, the assembly of NPs in these aerogels still, at least partially, relies on the interaction of organic assisting agents. Therefore, a genuine case of assembling high-purity aerogels from inorganic-only building blocks is still lacking.

In recent years, two-dimensional (2D) nanosheets, such as MnO₂, MoS₂, BN, and so forth, have emerged as interesting functional materials,³²⁻⁴⁰ exhibiting large specific area and strong self-assembly as a result of van der Waals force, hydrogen bonding, *etc.*, and thus, have offered promising starting building blocks to assemble pure inorganic aerogels. However, due to the difficulty and/or limited options of manipulating inorganic interaction,^{1, 41} it remains a grand challenge to control inorganic assembling process and force these nanosheets into desired 3D structures.

In this contribution, we have successfully self-assembled a high-purity inorganic aerogel via ice-templating starting from monodispersed organic-free 2D MnO₂ nanosheets. To our best knowledge, it is the first reported case of achieving pure inorganic aerogel from preformed NPs without using any functionalization or stabilization agents. The resultant MnO₂ aerogels are also with extremely low density (as low as ~0.53 mg cm⁻³), being the lightest metal oxide aerogel to date. The successful formation of the aerogel can be attributed to the enhanced van der Waals force between the 2D building blocks that have been more closely and more orderly arranged by squeezing ice crystals during freezing process, demonstrating a novel approach to construct inorganic aerogels only relying on weak interactions. It has also been shown that the obtained MnO₂ aerogel can function as an effective absorbent for toxic reducing gas, owing to its strong oxidation ability and high porosity. The herein presented strategy holds good potential to be applied to the fabrication of other high-purity inorganic aerogels, especially for those with 2D building blocks readily available.

Results and discussion

High-purity MnO₂ aerogels were self-assembled from monodispersed MnO₂ nanosheets by fully manipulating the interaction between inorganic NPs via an ice-templating approach. The building blocks of MnO₂ nanosheet, which displayed a 2D morphology with a lateral dimension mainly in the range of 170 to 240 nm and a typical thickness of 2~4 nm (Fig. 1a, S4[†] and S5[†]), were obtained by ultrasound-exfoliation of purified layered MnO₂ nanosheets following our reported method with minor modification (See S2.1[†] for details).^{42, 43} Then the colloid of organic-free building blocks (inset of Fig. 1a) was cultivated at a temperature (-20 °C) below the freezing point to form a 3D network as confined by the growing ice crystals. A free-standing cylindrical MnO₂ aerogel can be obtained by the sublimation of ice in a freeze-dryer, which is light enough to stand on a dandelion without damaging it (inset of Fig. 1b). The obtained aerogel exhibits a biomimetic foam structure with interconnected macro-pores that can be distinguished by naked eyes. Subsequent measurement shows

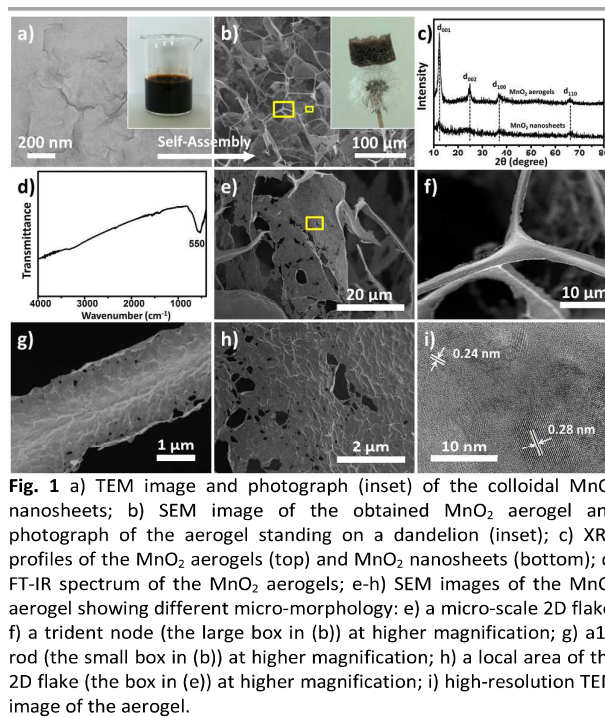


Fig. 1 a) TEM image and photograph (inset) of the colloidal MnO₂ nanosheets; b) SEM image of the obtained MnO₂ aerogel and photograph of the aerogel standing on a dandelion (inset); c) XRD profiles of the MnO₂ aerogels (top) and MnO₂ nanosheets (bottom); d) FT-IR spectrum of the MnO₂ aerogels; e-h) SEM images of the MnO₂ aerogel showing different micro-morphology: e) a micro-scale 2D flake; f) a trident node (the large box in (b)) at higher magnification; g) a 1D rod (the small box in (b)) at higher magnification; h) a local area of the 2D flake (the box in (e)) at higher magnification; i) high-resolution TEM image of the aerogel.

a density around 1.0 mg cm⁻³ (*i.e.* 4.4 mg in 4.4 cm³, Fig. S7[†]) and a high porosity of ~99.9%, indicating the successful formation of an ultralight material ($\rho < 10$ mg cm⁻³).^{44, 45} The microstructure of the aerogel has been further characterized by scanning electron microscopy (SEM), which reveals a 3D percolating network with open pores ranging from hundreds of nanometres to tens of micrometres (Fig. 1b), confirming the self-assembly from nanoscale into macroscopic structure.

The X-ray diffraction (XRD) peaks of the MnO₂ building blocks (bottom curve in Fig. 1c) can be indexed to δ -MnO₂ (JCPDS No. 18-0802) and the broad and low intensity XRD peaks indicate a poor crystalline or polycrystalline feature.⁴⁶ The self-assembled aerogel (upper curve in Fig. 1c) shows characteristic peaks (d_{001} , d_{002} , d_{100} and d_{110}) at the same positions as those of starting MnO₂ nanosheets. It should be noted that the interlayer peaks (corresponding to d_{001} and d_{002}) of the aerogel are sharper and stronger, suggesting higher crystallinity of the MnO₂ assembly and more ordered arrangement of nanosheets conferred by ice-templating.^{10, 47, 48}

The Fourier transform infrared (FT-IR) spectrum of the aerogel (Fig. 1d) only exhibits an evident band at 550 cm⁻¹, which can be assigned to the vibrations of octahedral [MnO₆] framework, and no characteristic bands of organic compounds can be identified. Corroboratively, the elemental analysis of the MnO₂ nanosheets (See S2.2[†] for details) shows no potential organic elements (C and S), whereas only trace amount of Na and K, representing inherent balancing cations, has been detected in addition to Mn and H. It has been found from literature that reported inorganic aerogels assembled from preformed NPs normally require organic components to

Tab. 1 Comparison of purity and assembling force for recently reported aerogels assembled from preformed inorganic NPs.

Reported aerogels	Preformed building blocks	Organic additives	Methods	Assembling Force		Impurities	Ref.
BaTiO ₃ aerogels	BaTiO ₃ nanoparticles	2-[2-(2-methoxyethoxy)ethoxy] acetic acid	Organic functionalized gelation	Organic interaction	Hydrogen bonding between the acetic acid	Acetic acid residue	18
Si/Ag/MnO ₂ aerogels	Si/Ag/MnO ₂ nanowires	Sodium dodecyl benzene sulfonate (SDBS)	Condensation assisted gelation		Van der Waals force between SDBS	SDBS residue	23
MoS ₂ /BN aerogels	MoS ₂ /BN nanosheets	Sodium cholate (SC)	Condensation assisted gelation		Van der Waals force between SC	SC residue	23
Ag/Cu aerogels	Ag/Cu nanowires	Polyvinylpyrrolidone (PVP)	Ice-templated assembly		Van der Waals force between PVP	PVP residue	29,31
MnO ₂ aerogels	MnO ₂ nanoflowers	Dimethylformamide (DMF)	Ice-templated assembly		Van der Waals force & hydrogen bonding between DMF	DMF residue	30
Ag hydrogels/aerogels	Ag nanoshells	Thiolate (glutathione)	Oxidative aggregation	Inorganic interaction	Fuse together between Ag	Thiolate residue	24
Pnictide aerogels	Pnictide nanoparticle	11-mercaptoundecanoic acid	Oxidative aggregation		Fuse together between pnictide	Thiolate residue	17
Chalcogenide aerogels	Metal Chalcogenide nanoparticle	4-fluorophenylthiolate	Oxidative aggregation		Fuse together between chalcogenide	Thiolate residue	20
MnO ₂ aerogels	Monodispersed MnO ₂ nanosheets	None	Ice-templated assembly		Van der Waals force between MnO ₂ nanosheets	No organics detected	This work

assist the assembly and usually contain organic residues as a result (Tab. 1). Thus, to our best knowledge, it is the first reported case of achieving organic-free inorganic aerogels from performed NPs without using any functionalization or stabilization agents.

The micro-morphology of the MnO₂ aerogel was examined in more details by SEM and transmission electron microscopy (TEM). It has been found that the 3D network of the aerogel consists of two major types of microstructures: one-dimensional (1D) rods and 2D flakes, as revealed in both the top-view and sectional-view SEM images (Fig. 1b and S8†). The average length of the 1D rods is estimated as ~50 μm, whereas the 2D flakes show a lateral dimension of ~50 μm (Fig. 1e and S9†). Many “Y-shaped” trident nodes, made of three joined 1D rods, can be found in the SEM images (Fig. 1f and S10†) and these 1D rods usually possess a prismatic shape with concaved sides (Fig. 1g and S10†). SEM and TEM images of higher magnification show that both 1D rods (Fig. 1g and S11a†) and 2D flakes (Fig. 1h and S11†) exhibit multiple wrinkles, presumably as a result of stacked nanosheets. It is noteworthy that the perceived average lateral dimensions of the nanosheets in 1D rods and 2D flakes are ~200 nm (Fig. S11†), which are in good agreement with the observed size for the building blocks of colloidal MnO₂ nanosheets (Fig. 1a and S4†). Moreover, the high-resolution TEM image (Fig. 1i) reveals that the obtained MnO₂ aerogels are polycrystalline and the lattice fringes show *d*-spacing of 0.24 nm and 0.28 nm, corresponding to the *d* values of (100) and (110) planes of δ-MnO₂, respectively. Therefore, the obtained 3D aerogel demonstrates a hierarchical structure, that is, the 3D network is constructed of 1D rods and 2D flakes, which have been assembled from MnO₂ nanosheets.

The concentrating and squeezing effect afforded by ice-templating has been proposed here as the major mechanism that controls the formation of the aerogel and determines the resultant morphology.²⁸ When the liquid of MnO₂ colloids freezes below the freezing point, nucleation of ice crystals will occur randomly on the frozen surface of the colloid. Then, ice

nuclei gradually grow in the MnO₂ colloids, eventually reaching a regime of cellular morphology.²⁸ MnO₂ nanosheets, excluded from the ice crystals at the early stage of freezing, are repelled and concentrated by the growing ice crystals (Fig. 2a). Therefore, the solidifying body can be divided into two domains: particle-free regions, corresponding to the cellular ice crystals free of nanosheets, and particle-rich regions, corresponding to the concentrated nanosheets excluded by ice. Subsequently, the nanosheets in the particle-rich region start aggregation and form a 3D network confined by the growing ice crystals, which result in the microstructures of 1D rods and 2D flakes. This hypothetical mechanism can be supported by the findings of glaciology research. As revealed in the works of glaciology,⁴⁹ an interconnected system of water-filled veins (Fig. 2b) can form in polycrystalline ice at a temperature near but below the freezing point. The veins lie along the lines where three ice grains meet and are squeezed by these ice grains from three sides. As a consequence, the veins usually take on a shape of a curved-in prism (Fig. 2c), which may explain the concave prismatic morphology of 1D rods in this work (Fig. 1g). The junction of two veins usually merges one vein into another and results in a “Y-shaped” trident node (Fig. 2b), as observed by SEM (Fig. 1f). Similar observation has also been made by Chen’s group for the self-assembled Au NPs directed by polycrystalline ice.⁵⁰ Furthermore, at the interface of two ice grains instead of three, 2D flakes (Fig. 1e) can be formed in the cleavage between the surfaces of two ice grains, which is also in line with the mechanism proposed by other groups.^{10, 31}

In order to verify that the microstructures of 1D rods and 2D flakes were formed by the concentrating and squeezing effect of ice during freezing process, the icy chunk of the frozen colloid was thawed at room temperature and characterized by SEM. In contrast to the homogeneous colloid before freezing, the freeze-thawed sample shows colourless liquid with a large amount of brown sediments at the bottom (Fig. S14†), indicating that the nanosheets have aggregated during freezing. The SEM image of the sediments obtained

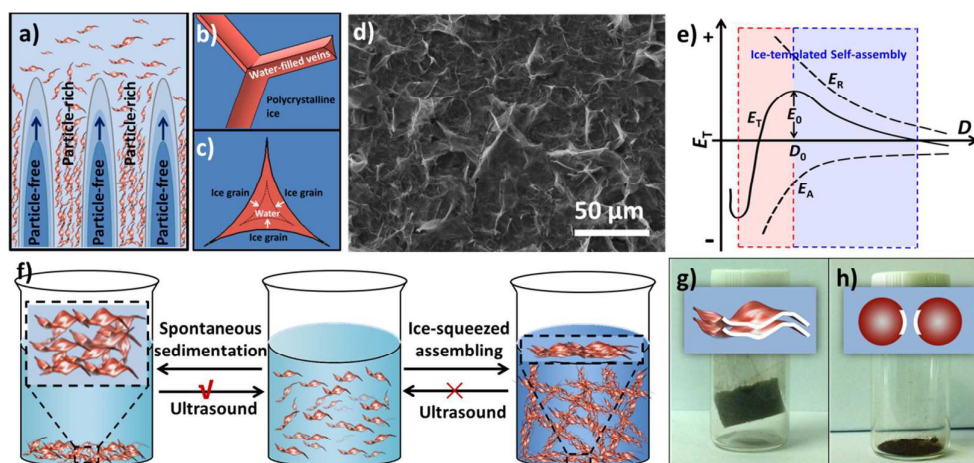


Fig. 2 a) Schematic diagram demonstrating the growth of ice crystals in the MnO_2 colloid during freezing process; b) schematic illustration of water-filled veins in polycrystalline ice, showing a “Y-shaped” trident node as a result of merging one vein into another at a junction of two veins; c) cross-section illustration of a vein exhibiting a shape of a concave-faced prism; d) SEM image of the sediments obtained from the freeze-thawed MnO_2 colloid at 1.0 mg mL^{-1} ; e) theoretical illustration of the relationship between the energy (E_T , E_A and E_R) and the distance (D) between NPs during ice-templated assembly; f) schematic illustration for ultrasound treatment of spontaneous sediments (left) and ice-squeezed assembly (right); g-h) schematic (top) and photographic (bottom) illustrations of ice-templated assembly obtained from MnO_2 nanosheets (g) and MnO_2 nanospheres (h).

from the freeze-thawed MnO_2 colloid (1.0 mg mL^{-1}) displays abundant 2D flakes accompanied with a few 1D rods (Fig. 2d and S15[†]), which is consistent with the SEM image of the aerogel (Fig. 1b). This observation suggests that the 1D rods and 2D flakes of the aerogel are indeed formed by the ice-templating effect on MnO_2 nanosheets before the sublimation of ice and a gentle ice removal (*i.e.* freeze-drying) is crucial to preserve the 3D network assembled in the freezing process.

Based on the Derjaguin-Landau-Verwey-Overbeek (DLVO) theory,^{51, 52} the stability of NPs in solution is mainly determined by the balance between two factors, namely, repulsive force and attractive force. As shown in Fig. 2e, the total potential energy (E_T) can be expressed as:

$$E_T = E_R + E_A \quad (1)$$

where E_R is the repulsive energy (usually positive in value) and E_A is the attractive energy (usually negative in value).

Our MnO_2 nanosheets demonstrate a zeta potential around -10 mV and can form an aqueous colloid due to the electrostatic repulsion of the negative charge on their surface (Fig. S6[†]).^{53, 54} When ice crystals nucleate and gradually grow in the colloid, the MnO_2 nanosheets are squeezed into a closer proximity and the van der Waals force between adjacent nanosheets increases, leading to a more negative value of E_A (Fig. 2e). Simultaneously, the repulsion between the negatively charged nanosheets will also elevate. However, the balancing cations (H_3O^+ , Na^+ and K^+), also excluded and concentrated by the expanding ice crystals, can change the ionic atmosphere of the nanosheets and partially mitigate the rising repulsion between the negatively charged surfaces as they approach each other. As a result, although both E_A and E_R increase in absolute value (E_A is more negative in value), as the distance

(D) between nanosheets decreases, E_A surges up in absolute value more quickly than E_R . Therefore, whereas E_R dominates over E_A in increment as ice crystals start to reduce D , the net incremental effect on E_T becomes zero at a certain critical point (D_0), because the increment of E_R is neutralized by the increment of E_A . As a consequence, E_T reaches its maxima (E_0) and sets off a course of self-declining once it overcomes E_0 , which further reduces D ($D < D_0$) till steric hindrance stops it. At the macroscopic level, a stable assembly of nanosheets can be achieved as E_T declines.

It should be noted that the ice-squeezing effect plays a critical role in forming the stable assembly of 2D nanosheets, especially due to its rearrangement of the squeezed nanosheets. It has been found that the spontaneous sediments driven by gravity can be easily sonicated into a homogenous colloid by ultrasound-treatment (100 W) of a few seconds, whereas the freeze-thawed sediments from ice-squeezed assembly can no longer be redispersed into a colloid under the same ultrasound-treatment even for a longer period of 30 minutes (Fig. S14[†]), indicating the formation of a stable assembly. Such an observation is probably caused by two coordinated actions of squeezing ice (Fig. 2f). On one hand, growing ice crystals concentrate nanosheets and balancing cations as discussed above. On the other hand, the squeezing of ice crystals also aligns nanosheets more orderly, as evidenced by the XRD profile of the aerogel (Fig. 1c), and leads to more effective surface for van der Waals interaction. As a consequence, the resultant ice-squeezed assembly requires more energy input than spontaneously sedimented nanosheets to overcome a higher energy barrier to disassemble, and thus is more stable.

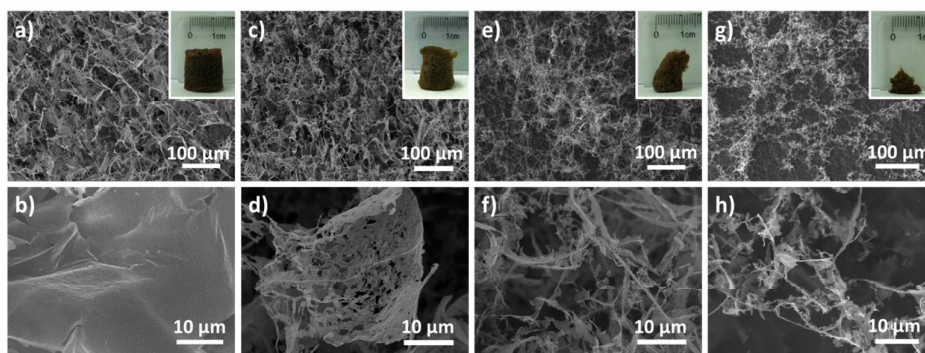


Fig. 3 Top-view SEM images of MnO₂ aerogels prepared from nanosheet colloids of different concentrations: a-b) 1.0 mg mL⁻¹, c-d) 0.5 mg mL⁻¹, e-f) 0.25 mg mL⁻¹ and g-h) 0.1 mg mL⁻¹. The inset images in a), c), e) and g) are the photographs of corresponding aerogels. The bottom images of b), d), f) and h) are higher magnification images of a), c), e) and g), respectively.

As a direct inference of the above explanation, large effective surface for van der Waals attraction as afforded by 2D nanosheets is critical to the successful formation of the aerogel (Fig. 2g). To this end, MnO₂ nanospheres with smaller effective surface for van der Waals interaction was chosen as the building blocks to construct aerogels under otherwise identical conditions as used for 2D MnO₂ nanosheets (See S4.2 † for details). After the removal of the ice, the 3D network of the frozen colloid collapsed into a powder instead of forming an aerogel (Fig. 2h and S17 †), indicating that the van der Waals force between nanospheres is weak and cannot provide adequate strength to maintain the 3D architecture.

Encouraged by the successful construction of ultralight aerogel with a density of 1.0 mg cm⁻³, we set out to explore whether MnO₂ aerogels with even lower density could be achieved. Parallel aerogel formation with different concentrations of MnO₂ nanosheet colloids (1.0, 0.5, 0.25 and 0.1 mg mL⁻¹) had been observed by naked eyes and SEM (Fig. 3). It has been found that the obtained MnO₂ aerogels exhibit a trend of more collapsing with decreasing colloidal concentration (insets of Fig. 3a, 3c, 3e and 3g). Free-standing MnO₂ aerogels of the container shape can be formed without evident collapsing at the concentrations of 1.0 and 0.5 mg mL⁻¹ (insets of Fig. 3a and 3c), whereas the colloidal concentrations of 0.25 and 0.1 mg mL⁻¹ result in obvious defects of aerogels (insets of Fig. 3e and 3g). The density of the MnO₂ aerogel constructed from the colloid of 0.5 mg mL⁻¹ is estimated as ~0.53 mg cm⁻³ (See S2.3 † for the details of estimation method), which is the lowest reported density for metal oxide aerogels to our best knowledge. As a matter of fact, in the ultralight regime below 1 mg cm⁻³, only few materials are currently known: metallic microlattices ($\rho \geq 0.87$ mg cm⁻³),^{44,45} aerographite ($\rho \geq 0.18$ mg cm⁻³),⁵⁵ graphene aerogels ($\rho \geq 0.16$ mg cm⁻³),¹⁴ and polyacrylonitrile/silica hybrid aerogels ($\rho \geq 0.12$ mg cm⁻³),⁵⁶ etc. Our MnO₂ aerogel ($\rho \geq 0.51$ mg cm⁻³) adds the first member of metal oxide to the family of ultralight materials below 1 mg cm⁻³.

We next investigated the concentration dependence of the aerogel micro-morphology by SEM to elucidate the hierarchy of the 3D structure. It has been discovered that not only can more 2D flakes and less 1D rods be observed at higher

concentration of starting MnO₂ colloid (Fig. 3b and 3d compared to 3f and 3h), but also less defects can be found on the 2D flakes formed from higher colloid concentration (Fig. 3b compared to 3d). Although 1D rods can be viewed as extremely defected cases of 2D flakes, they coexist at a concentration even as low as 0.1 mg mL⁻¹ (Fig. 3h), where the aerogel formed has demonstrated significant collapsing. Hence, it has been proposed that during the formation of our aerogels, MnO₂ nanosheets assemble into 1D rods and 2D flakes simultaneously, which are subsequently connected to form 3D compartmental networks. In addition, the fractions of 1D rods and 2D flakes can be tuned by altering the concentration of starting nanosheet colloid. It is conceivable that below a critical concentration it is difficult for NPs to form sufficient 1D and 2D building blocks to maintain a well-shaped 3D network.

MnO₂ is known for its oxidation ability and can be used as absorbent for reducing toxicants.⁵⁷ Thus, we set up a simple experiment to explore the potential to utilize our MnO₂ aerogels to adsorb toxic reducing gas. In particular, hydrazine (N₂H₄) was chosen for its easy evaporation form N₂H₄·H₂O liquid at low temperature. The colour of MnO₂ aerogels has gradually changed from dark brown (Fig. 4a) into yellow (Fig. 4b) as the hydrazine gas is being produced at 60 °C, indicating that the hydrazine vapour generated has indeed been absorbed by the aerogel. The colour change of the aerogels can be attributed to the transformation of MnO₂ into Mn(OH)₂ by the reducing gas.⁵⁸ Then a reported N₂H₄-sensitive colorimetric probe (Fig. 4c), prepared according to previously reported method,⁵⁸ has been used for the detection of residual hydrazine to verify the adsorption efficiency of MnO₂ aerogels. No evident colour change of the colorimetric probe has been observed (top inset of Fig. 4d) and no significant change of absorption could be detected from the UV-vis spectrum (top line in Fig. 4d compared to pre-absorption curve in Fig. 4c), indicating that the hydrazine gas has been almost completely absorbed by MnO₂ aerogels. In contrast, in the absence of any absorbents, the yellow colour of colorimetric probe quickly faded (bottom inset of Fig. 4d) and the absorption peak at 374 nm, the characteristic peak of the probe, was lost (bottom line

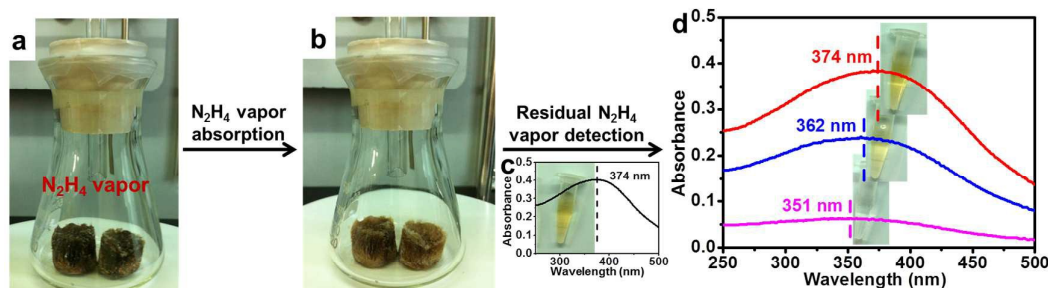


Fig. 4 MnO₂ aerogels as effective absorbents for N₂H₄ vapor. a) Photograph of the pre-absorption MnO₂ aerogels: two pieces of dark brown MnO₂ aerogels were placed in the conical flask where N₂H₄ vapor would be produced by heating; b) Photograph of the MnO₂ aerogels after hydrazine absorption showing the color of the aerogel changed into yellow; c) UV-Vis spectrum and photograph (inset) of the colorimetric probe, which is 5 µg/mL colloidal suspension of MnO₂ nanosheets as previously reported; d) UV-Vis spectra and photographs (inset) of the colorimetric probes after the detection of residual hydrazine: top curve (red) and inset are for the probe used in the detection of gas generated in presence of MnO₂ aerogels, middle curve (blue) and inset are for the probe used in the detection of gas generated in presence of MnO₂ powders, bottom curve (purple) and inset are for the probe used in the detection of gas generated in absence of absorbents.

in Fig. 4d). As a control, commercial MnO₂ (c-MnO₂) powders, have also been tested as the absorbents under otherwise identical conditions. The colour of colorimetric probe changed from yellow to light yellow (middle inset of Fig. 4d). Meanwhile, peak shift (from 374 nm to 362 nm) and substantial decrease in absorption have been found in the UV-vis spectrum (middle line in Fig. 4d). Together our MnO₂ aerogels has demonstrated superior absorption efficiency than MnO₂ powders, and is a better candidate for applications of reducing gas absorption.

Conclusions

In conclusion, it has been demonstrated that a high-purity inorganic aerogel can be assembled from 2D nanosheets via ice-templating without using any extra functionalization or cross-linking agents, which only relies on the weak interactions between NPs. The MnO₂ aerogels are simply prepared by freeze-drying the frozen colloids of 2D building blocks and the aerogels achieved exhibit a density as low as ~0.53 mg cm⁻¹, recruiting the first member of metal oxide into the ultralight material family ($\rho < 1.0$ mg cm⁻³). The resultant morphology and microstructures of the aerogel (e.g. 1D rods and 2D flakes) are in good consistency with the ice forming mechanism as learned from glaciology. The successful formation of the aerogel can be attributed to the enhanced van der Waals force between the 2D building blocks that have been more closely and more orderly arranged by squeezing ice crystals during freezing process. It has also been demonstrated that the obtained MnO₂ aerogel can function as an effective absorbent for toxic reducing gas, owing to its strong oxidation ability and high porosity. The ice-templating approach presented here provides a general strategy that holds good potential to be applied to the fabrication of other high-purity inorganic aerogels, especially for those with 2D building blocks readily available.

Acknowledgements

This work was supported by National Natural Science Foundation of China (21471067, 51402121, 51302103 and 51375204) and Jilin Provincial Science & Technology Department (20140520101JH, 20140520163JH and 20140101056JC).

Notes and references

- Z. H. Nie, A. Petukhova and E. Kumacheva, *Nat. Nanotechnol.*, 2010, **5**, 15-25.
- G. M. Whitesides and B. Grzybowski, *Science*, 2002, **295**, 2418-2421.
- M. Grzelczak, J. Vermant, E. M. Furst and L. M. Liz-Marzan, *ACS Nano*, 2010, **4**, 3591-3605.
- S. S. Kistler, *Nature*, 1931, **127**, 741.
- A. C. Pierre and G. M. Pajonk, *Chem. Rev.*, 2002, **102**, 4243-4265.
- H. D. Gesser and P. C. Goswami, *Chem. Rev.*, 1989, **89**, 765-788.
- N. Hüsing and U. Schubert, *Angew. Chem. Int. Ed.*, 1998, **37**, 22-45.
- H. C. Bi, Z. Y. Yin, X. H. Cao, X. Xie, C. L. Tan, X. Huang, B. Chen, F. T. Chen, Q. L. Yang, X. Y. Bu, X. H. Lu, L. T. Sun and H. Zhang, *Adv. Mater.*, 2013, **25**, 5916-5921.
- Z. S. Wu, S. B. Yang, Y. Sun, K. Parvez, X. L. Feng and K. Mullen, *J. Am. Chem. Soc.*, 2012, **134**, 9082-9085.
- L. Estevez, A. Kelarakis, Q. M. Gong, E. H. Da'as and E. P. Giannelis, *J. Am. Chem. Soc.*, 2011, **133**, 6122-6125.
- J. K. Yuan, X. G. Liu, O. Akbulut, J. Q. Hu, S. L. Suib, J. Kong and F. Stellacci, *Nat. Nanotechnol.*, 2008, **3**, 332-336.
- S. M. Jung, H. Y. Jung, W. J. Fang, M. S. Dresselhaus and J. Kong, *Nano Lett.*, 2014, **14**, 1810-1817.
- Y. Li, Z. Y. Fu and B. L. Su, *Adv. Funct. Mater.*, 2012, **22**, 4634-4667.
- H. Y. Sun, Z. Xu and C. Gao, *Adv. Mater.*, 2013, **25**, 2554-2560.
- Y. Long, J. F. Hui, P. P. Wang, S. Hu, B. Xu, G. L. Xiang, J. Zhuang, X. Q. Lu and X. Wang, *Chem. Commun.*, 2012, **48**, 5925-5927.
- M. A. Worsley, P. J. Pauzauskie, T. Y. Olson, J. Biener, J. H. Satcher and T. F. Baumann, *J. Am. Chem. Soc.*, 2010, **132**, 14067-14069.
- A. Hitihami-Mudiyanselage, K. Senevirathne and S. L. Brock, *ACS Nano*, 2013, **7**, 1163-1170.

18. F. Rechberger, F. J. Heiligtag, M. J. Suess and M. Niederberger, *Angew. Chem. Int. Ed.*, 2014, **53**, 6823-6826.
19. J. L. Mohanan, I. U. Arachchige and S. L. Brock, *Science*, 2005, **307**, 397-400.
20. S. Bag, P. N. Trikalitis, P. J. Chupas, G. S. Armatas and M. G. Kanatzidis, *Science*, 2007, **317**, 490-493.
21. W. Liu, A. K. Herrmann, N. C. Bigall, P. Rodriguez, D. Wen, M. Oezaslan, T. J. Schmidt, N. Gaponik and A. Eychmuller, *Acc. Chem. Res.*, 2015, **48**, 154-162.
22. H. Huang, P. W. Chen, X. T. Zhang, Y. Lu and W. C. Zhan, *Small*, 2013, **9**, 1397-1404.
23. S. M. Jung, H. Y. Jung, M. S. Dresselhaus, Y. J. Jung and J. Kong, *Sci. Rep.*, 2012, **2**, 849.
24. X. N. Gao, R. J. Esteves, T. T. H. Luong, R. Jaini and I. U. Arachchige, *J. Am. Chem. Soc.*, 2014, **136**, 7993-8002.
25. N. C. Bigall, A. K. Herrmann, M. Vogel, M. Rose, P. Simon, W. Carrillo-Cabrera, D. Dorfs, S. Kaskel, N. Gaponik and A. Eychmuller, *Angew. Chem. Int. Ed.*, 2009, **48**, 9731-9734.
26. S. Deville, E. Saiz, R. K. Nalla and A. P. Tomsia, *Science*, 2006, **311**, 515-518.
27. H. F. Zhang, I. Hussain, M. Brust, M. F. Butler, S. P. Rannard and A. I. Cooper, *Nat. Mater.*, 2005, **4**, 787-793.
28. S. Deville, E. Maire, G. Bernard-Granger, A. Lasalle, A. Bogner, C. Gauthier, J. Leloup and C. Guizard, *Nat. Mater.*, 2009, **8**, 966-972.
29. Y. Tang, K. L. Yeo, Y. Chen, L. W. Yap, W. Xiong and W. L. Cheng, *J. Mater. Chem. A*, 2013, **1**, 6723-6726.
30. S. Chen, G. X. Liu, H. Yadegari, H. H. Wang and S. Z. Qiao, *J. Mater. Chem. A*, 2015, **3**, 2559-2563.
31. H. L. Gao, L. Xu, F. Long, Z. Pan, Y. X. Du, Y. Lu, J. Ge and S. H. Yu, *Angew. Chem. Int. Ed.*, 2014, **53**, 4561-4566.
32. V. Nicolosi, M. Chhowalla, M. G. Kanatzidis, M. S. Strano and J. N. Coleman, *Science*, 2013, **340**, 1226419.
33. J. N. Coleman, M. Lotya, A. O'Neill, S. D. Bergin, P. J. King, U. Khan, K. Young, A. Gaucher, S. De, R. J. Smith, I. V. Shvets, S. K. Arora, G. Stanton, H. Y. Kim, K. Lee, G. T. Kim, G. S. Duesberg, T. Hallam, J. J. Boland, J. J. Wang, J. F. Donegan, J. C. Grunlan, G. Moriarty, A. Shmeliov, R. J. Nicholls, J. M. Perkins, E. M. Grieveson, K. Theuwissen, D. W. McComb, P. D. Nellist and V. Nicolosi, *Science*, 2011, **331**, 568-571.
34. Z. Q. Sun, T. Liao, Y. H. Dou, S. M. Hwang, M. S. Park, L. Jiang, J. H. Kim and S. X. Dou, *Nat. Commun.*, 2014, **5**, 3813.
35. X. Huang, Z. Y. Zeng and H. Zhang, *Chem. Soc. Rev.*, 2013, **42**, 1934-1946.
36. C. L. Tan and H. Zhang, *Chem. Soc. Rev.*, 2015, **44**, 2713-2731.
37. H. Li, J. M. T. Wu, Z. Y. Yin and H. Zhang, *Acc. Chem. Res.*, 2014, **47**, 1067-1075.
38. X. Huang, C. L. Tan, Z. Y. Yin and H. Zhang, *Adv. Mater.*, 2014, **26**, 2185-2204.
39. M. Chhowalla, Z. F. Liu and H. Zhang, *Chem. Soc. Rev.*, 2015, **44**, 2584-2586.
40. H. Zhang, *ACS Nano*, 2015, DOI: 10.1021/acsnano.1025b05040.
41. Y. J. Min, M. Akbulut, K. Kristiansen, Y. Golan and J. Israelachvili, *Nat. Mater.*, 2008, **7**, 527-538.
42. Z. Liu, K. Xu, H. Sun and S. Yin, *Small*, 2015, **11**, 2182-2191.
43. H. Sun, K. Xu, M. Huang, Y. Shang, P. She, S. Yin and Z. Liu, *Appl. Surf. Sci.*, 2015, **357**, 69-73.
44. X. Y. Zheng, H. Lee, T. H. Weisgraber, M. Shusteff, J. DeOtte, E. B. Duoss, J. D. Kuntz, M. M. Biener, Q. Ge, J. A. Jackson, S. O. Kucheyev, N. X. Fang and C. M. Spadaccini, *Science*, 2014, **344**, 1373-1377.
45. T. A. Schaedler, A. J. Jacobsen, A. Torrents, A. E. Sorensen, J. Lian, J. R. Greer, L. Valdevit and W. B. Carter, *Science*, 2011, **334**, 962-965.
46. S. Devaraj and N. Munichandraiah, *J. Phys. Chem. C*, 2008, **112**, 4406-4417.
47. H. Nishihara, S. R. Mukai, D. Yamashita and H. Tamon, *Chem. Mater.*, 2005, **17**, 683-689.
48. H. Y. Ma, Y. Gao, Y. H. Li, J. Gong, X. Li, B. Fan and Y. L. Deng, *J. Phys. Chem. C*, 2009, **113**, 9047-9052.
49. H. M. Mader, *Observations of the water-vein system in polycrystalline ice*, International Glaciological Society, Cambridge, ROYAUME-UNI, 1992.
50. X. S. Shen, L. Y. Chen, D. H. Li, L. F. Zhu, H. Wang, C. C. Liu, Y. Wang, Q. H. Xiong and H. Y. Chen, *ACS Nano*, 2011, **5**, 8426-8433.
51. B. V. Derjaguin, *Acta Physicochim. USSR*, 1941, **14**, 633-662.
52. E. J. W. Verwey, J. T. G. Overbeek and J. T. G. Overbeek, *Theory of the stability of lyophobic colloids*, Courier Corporation, 1999.
53. G. X. Zhao, J. X. Li, X. M. Ren, J. Hu, W. P. Hu and X. K. Wang, *RSC Adv.*, 2013, **3**, 12909-12914.
54. C. H. Chen, V. M. B. Crisostomo, W. N. Li, L. P. Xu and S. L. Suib, *J. Am. Chem. Soc.*, 2008, **130**, 14390-14391.
55. M. Mecklenburg, A. Schuchardt, Y. K. Mishra, S. Kaps, R. Adelung, A. Lotnyk, L. Kienle and K. Schulte, *Adv. Mater.*, 2012, **24**, 3486-3490.
56. Y. Si, J. Y. Yu, X. M. Tang, J. L. Ge and B. Ding, *Nat. Commun.*, 2014, **5**, 5802.
57. W. Y. Zhai, C. X. Wang, P. Yu, Y. X. Wang and L. Q. Mao, *Anal. Chem.*, 2014, **86**, 12206-12213.
58. Y. He, W. Huang, Y. Liang and H. Yu, *Sensor Actuat. B: Chem.*, 2015, **220**, 927-931.